Bone fracture analysis on the short rod chevron-notch specimens using the X-ray computer micro-tomography

R. DE SANTIS[1], P. ANDERSON[2], K. E. TANNER[3], L. AMBROSIO[1], L. NICOLAIS[1], W. BONFIELD[3]*, G. R. DAVIS[2]

[1]*Institute of Composite Materials Technology, National Research Council, and Interdisciplinary Research Centre in Biomaterials, University of Naples ''Federico II'', Piazzale Tecchio 80, 80125 Napoli, Italy*

[2]*Department of Biophysics in Relation to Dentistry, Queen Mary and Westfield College, University of London, London E1 4NS, U.K.*

[3]*Interdisciplinary Research Center in Biomedical Materials, Queen Mary and Westfield College, University of London, London E1 4NS, U.K.*

Mechanical fatigue of bone leads to micro-cracking which is associated with remodeling, establishing a balance in the microcrack population of the living tissue, thus, in the steady-state, the microstructure of bone provides sites of discontinuity acting as stress raisers. Hence fracture toughness plays a decisive role in bone functionality by determining the level to which the material can be stressed in the presence of cracks, or, equivalently, the magnitude of cracking which can be tolerated at a given stress level.

Cortical bone, which behaves as a quasi-brittle solid when fractured, was tested as short-rod chevron-notched tension specimens (CNT). The main features of the CNT specimen are its geometry and the V shaped notch. The notch leads to steady-state crack propagation whilst the requested geometry allows a diameter 40% smaller than the thickness of a standard compact tension specimens (CT). These features are essential to distinguish the inhomogeneties in the fracture properties of materials like bone.

Bone structure and crack propagation of the CNT specimens were analyzed using X-ray computed micro-tomography (XMT), which is a non-invasive imaging technique. The unique feature of the micro-CT is the high resolution three-dimensional image which consists of multi-sliced tomographs taken in a fine pitch along the rotational axis.

Fracture toughness (K_{IC}) computed according to the peak load was 4.8 $MNm^{-3/2}$ while that derived from experimental calibration tests using XMT was 4.9 $MNm^{-3/2}$.

Introduction

Bone undergoes micro-cracking as a result of mechanical fatigue while simultaneously the remodeling process occurs, establishing a balance in the microcrack population in the living tissue [1], thus, in the steady state, the microstructure of bone provides sites of discontinuity, including lacunae, canaliculi, blood vessels and muscle insertions, acting as stress raisers [2]. For instance vascular spaces approach the dimensions of intrinsic crack initiation sites [3]. A comparison between the fracture mechanism *in vitro* of both human and bovine cortical bone suggests that the microcracks which form around a crack-tip redistribute the stresses increasing the toughness of the material [4].

Haversian bone is similar in its osteonal arrangement and mechanical behavior to a tough discontinuous fiber reinforced laminate [5]. A ductile osteon-matrix interface (cement line) promotes crack initiation [6], but slows crack propagation in compact bone [7], by blunting the crack tip and trapping it within the lamellar structure, thus increasing fracture toughness [8]. Debonding of an osteon produces changes in the Haversian canal wall including interruption of streaming potentials and nutrient supply adjacent to the crack. This debonding initiates remodeling and production of a new secondary osteon, initially less calcified than the surrounding bone [8], which may act as a fiber reinforcement [7] preventing the accumulation of microdamage due to repetitive loading [9].

Micro-mechanical models of osteonal cortical bone suggest that the ratio of the modulus of the osteon to that of the interstitial bone controls crack propagation: newly

*Now at Department of Materials Science and Metallurgy, University of Cambridge, Pembroke Street, Cambridge, CB2 3QZ, UK.

formed, low-stiffness osteons may toughen cortical bone tissue by promoting crack propagation toward tougher osteons while stiff osteons repel the microcrack from more brittle osteons [10]. With ageing, microdamage occurs more rapidly than the intrinsic repair process [11]. The effects of this accumulation of microcracks, which is higher in female than male specimens [12], is reduced mechanical properties and increased fragility [13, 14]. Thus bone fracture has an increased occurrence within older populations since the microstructural organisation of bone controls the relationship between loading conditions and fracture patterns [6–9, 15]. Hence fracture toughness plays a decisive role in bone functionality by determining the level to which the material can be stressed in the presence of cracks, or, equivalently, the magnitude of cracking which can be tolerated at a given stress level.

In the last two decades fracture mechanics testing has been used to evaluate the fracture toughness of cortical bone by applying linear elastic fracture mechanics (LEFM). However the major effort in bone fracture studies *in vitro* concentrated on propagation of the crack, rather than its initiation, and in the direction parallel to the long axis of a long bone (longitudinal direction) using a variety of pre-cracked specimens: 3-point bending specimens [16], compact tension specimens (CT) [4, 5, 17–20], single edge-notched specimens (SEN) [20–22], center-notched cylindrical specimens (CNC) [20] and compact sandwich specimens [23].

The CT geometry proved to be the most useful for studying Mode I fracture mechanics of bone in the longitudinal direction (tensile opening mode in which the crack faces separate in a direction normal to the plane of the crack). The CT specimen is popular, despite difficulties with the dimensional requirements [24] in bone because of the curved cross-section of most long bones [25]. Moreover, because of bone anisotropy, the CT geometry is not intrinsically suitable for the analysis of bone fracture toughness in directions other than the longitudinal. Thus, V-grooves on both sides of CT bone specimens are essential to control the direction of crack growth when the specimen axis is not parallel to that of the bone [27]. Although the shear strength of bone is lower than the tensile strength, Mode II fracture mechanics (in-plane sliding mode in which the crack faces shear in a direction parallel to the crack growth) in the longitudinal direction suggests that resistance to crack growth in human cortical bone is greater in shear than in tension [19].

XMT is a 3-D X-ray microscopical technique developed over the past 15 years and it is a miniaturized version of the well known medical computer axial tomography method. The novel 4th generation [27] uses a 2-D CCD detector coupled to a scintillator to record the images specimens up to 40 mm in diameter using the transmitted X-ray beam from a laboratory source with a silver target. XMT yields the three dimensional image from which structural parameters can be derived [28, 29].

Materials and methods

Two shafts of fresh adult bovine femora (2 years old) were machined using a CN Lathe (Emco turn 120, Austria) and a diamond band saw (Exakt, Germany) cooled by chilled water, to the short rod CNT geometry [30] (Fig. 1). Specimens were tested according to ASTM B771-87 [30]. The main features of the CNT specimen are its geometry and the V shaped notch. The latter constrains the crack to steady-state propagation in the chevron-notch ligament whilst the former allows a diameter 40% smaller than the thickness of a standard CT specimen [24, 30, 31].

To grip the specimens in the mechanical testing machine and the micro-CT equipment, the standard specimens were slightly modified: the final configuration of the CNT was that of a 'top hat' where the load is transferred to the specimens using two stainless steel pins (Fig. 2) through the ''brim''. The main axis of each CNT bone specimen was aligned with the longitudinal direction of the femoral shaft. Specimens were stored wet at $-20\,^{\circ}\mathrm{C}$ until required. LEFM was applied to study fracture toughness of the short-rod CNT.

Mechanical tests were performed on 20 short rod CNT specimens, at room temperature, using a MTS 830 material testing system at the speed of $1.0 \cdot 10^{-3}\,\mathrm{mm} \cdot \mathrm{s}^{-1}$. Load and displacement data were digitally acquired at 4 Hz. High resolution video frames were acquired during each test using a Pulmix TM 1300 Video-camera connected to a PC Pentium. The progressive scanning frames were triggered by the MTS time signals. In order to obtain an unloading compliance 5 specimens underwent loading-unloading steps.

The apparent fracture toughness was computed from the equation [32]:

$$K_Q = A \cdot F_c / [D^{3/2} \cdot (1 - \nu^2)^{1/2}] \qquad (1)$$

where A is a dimensionless constant $(A = 20.8)$ which depends on geometry rather than the specimen material [32, 33]. F_c, which is the load at the crack length a_c, was taken to be the peak load reached during the mechanical tests, D is the diameter of the specimen and ν is the Poisson's ratio $(\nu = 0.28)$.

The apparent fracture toughness K_Q was corrected with a plasticity factor ρ, derived from the unloading compliance curves. The plasticity factor ρ was computed according to the equation [34]:

$$\rho = \Delta X_0 / \Delta X \qquad (2)$$

where the ratio $\Delta X_0 / \Delta X$ is calculated from the unloading compliance tests and ΔX_0 and ΔX are as shown in Fig. 3.

Hence the fracture toughness was determined according to the equation [34]:

$$K_I = K_Q \cdot [(1 + \rho)/(1 - \rho)]^{1/2} \qquad (3)$$

To analyze bone structure and to improve estimates of crack toughness and propagation, 5 CNT specimens underwent the XMT, which is a non-invasive imaging system [35, 36]. This new method of micro-image analysis is gaining attention in the biomechanical field due to its ability to measure accurately the mineral concentration. The unique feature of the XMT is the three-dimensional image which consists of multi-sliced tomographs taken at a fine pitch along the rotational axis. 3-D images of bone tissue may be developed with one

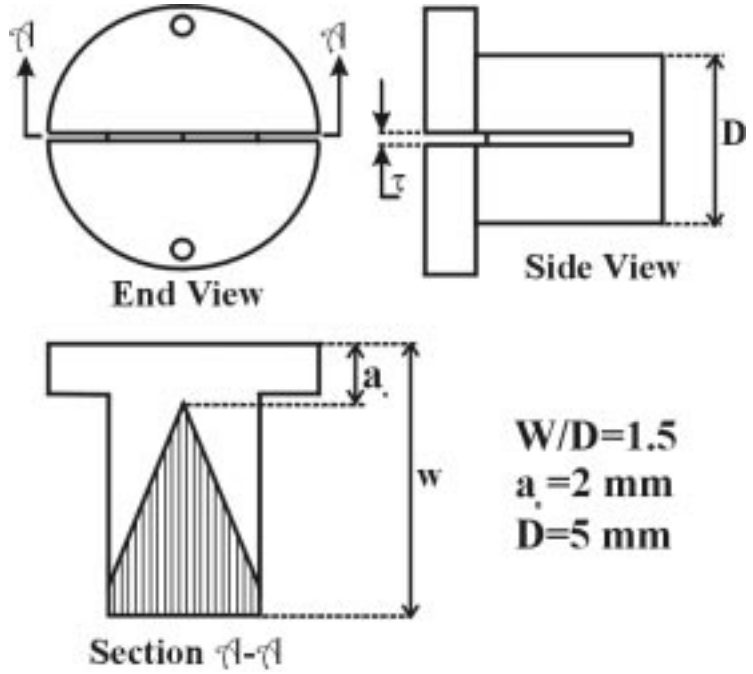

Figure 1 Short rod CNT specimen of bovine cortical bone.

micrometre resolution [36], from which structural parameters can be derived.

The micro-scanner, which is a miniaturized version of computerized axial tomography, used the time-delay integration method of imaging with a charge-coupled detector (CCD) [26, 37, 38] which records the intensity falling on an array 1024×512. Three-dimensional images of bone specimens, which consist of multi-sliced tomographs taken at a fine pitch along the CNT axis, were obtained with 40 μm resolution. This data was then fed into a computer program which produces 3D images of the sample. The 3D images were then sliced in both longitudinal and cross sections. Hence the geometrical properties are computed using the Corel 6.0 and NIH Image 1.57.

Displacement, load and crack length data were

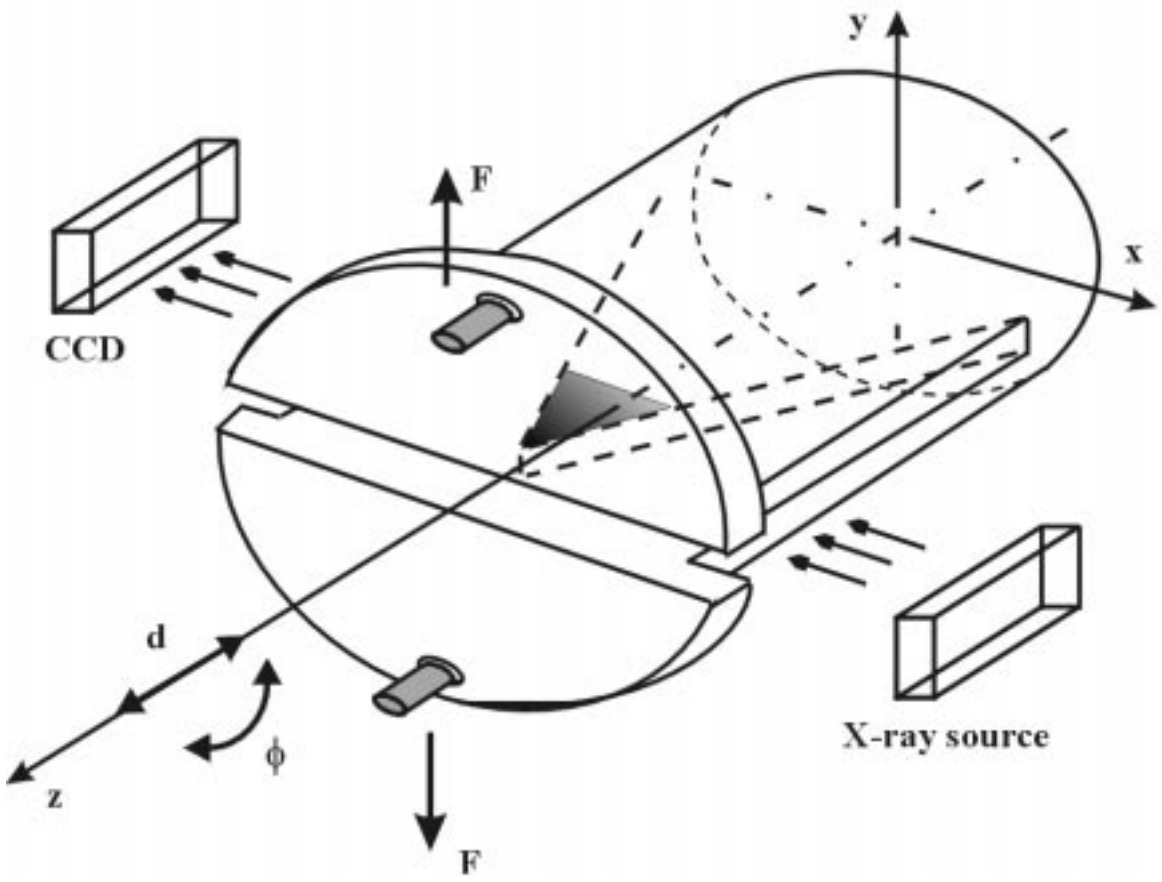

Figure 2 CNT specimen and X-ray CT testing system. ϕ and *d* are the relative movements between the CNT and the X-ray equipment frame. X-ray slices normal to the *z* axis and parallel to $\pi_{z,y}$ and $\pi_{z,x}$ planes (longitudinal planes) were used to analyze the behavior of CNT bone specimens.

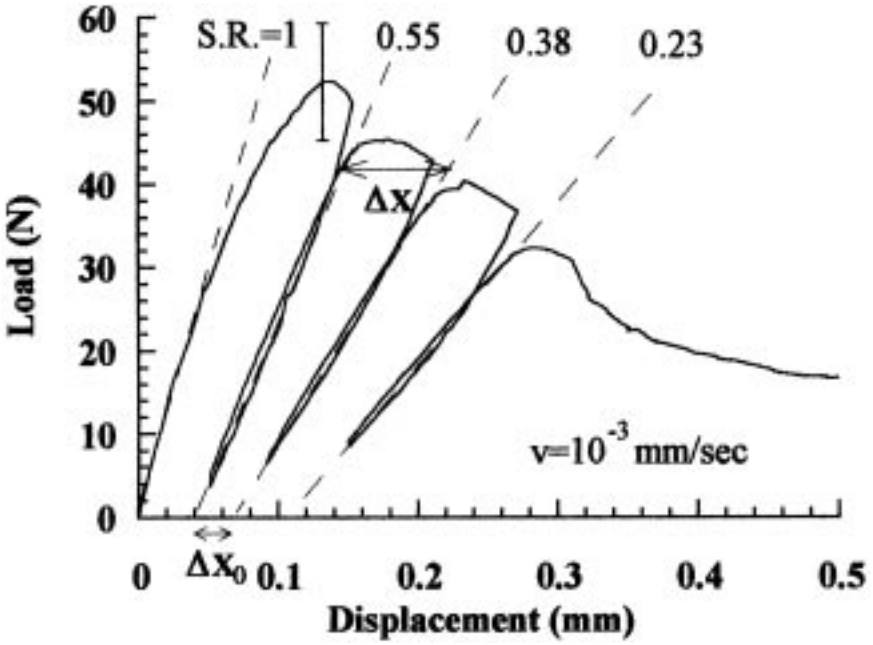

Figure 3 Loading-unloading compliance test. S.R. is the stiffness ratio. ΔX_0 and ΔX were used to compute the plasticity factor.

correlated in order to define the compliance behavior with the crack-length. Compliance data were expressed in the dimensionless form (C'):

$$C' = E' \cdot D \cdot C \tag{4}$$

where C is the compliance (the ratio between displacement and load); D is the specimen diameter;

$$E' = \begin{cases} E \text{ for plane stress} \\ \frac{E}{1-\nu^2} \text{ for plane strain} \end{cases}$$

and E is the elastic modulus.

The values used for the elastic modulus and the Poisson's ratio for bovine femoral cortical bone were $E = 23.9$ GPa and $\nu = 0.28$ respectively [39–40]. Plane strain and plane stress conditions characterize the immediate vicinity of the notch and the bulk of the CNT specimen respectively [41]. Therefore plane strain relations were used to compute the stress intensity factor from the compliance measurements.

Dimensionless compliance was then correlated to the dimensionless crack length $\alpha = a/w$ (where a is the crack front distance from the specimen edge and w the specimen length, Fig. 1). A fourth degree polynomial

$$\sum_{i=0}^{4} M_i \cdot \alpha^i \tag{5}$$

was used to fit the compliance data.

The polynomial function was then differentiated in order to compute the dimensionless stress intensity factor expressed by:

$$Y = \left[\frac{1}{2} \cdot \frac{dC'}{d\alpha} \cdot \frac{\alpha_1 - \alpha_0}{\alpha - \alpha_0}\right]^{\frac{1}{2}} \tag{6}$$

where α_0, α_1 are the dimensionless chevron-notch parameters $\alpha_0 = a_0/w$ (dimensionless initial crack length) and $\alpha_1 = a_1/w$ respectively.

The minimum value of Y, $Y_{\min}$, was then correlated to the critical mode I fracture toughness by the equation:

$$K_{Ic} = \left[\frac{P_{\max}}{D \cdot \sqrt{W}} \cdot Y_{\min}\right] \tag{7}$$

KaleidaGraph 3.0 software was used for mathematical computations.

Results

The maximum load reached during the mechanical tests (including the monotonic loading-unloading tests) was 57 N (st. dev. = 6.2, $F_{\max} = 70$ N and $F_{\min} = 48$ N). Hence, according to Equation 1 the apparent fracture toughness is $K_Q = 3.5\,\text{MN} \cdot \text{m}^{-3/2}$.

Fig. 3 shows the average behavior of the short rod CNT specimens according to the loading-unloading mechanical tests. The stiffness ratio (S.R), which is the ratio between the current stiffness and the original stiffness, is shown at the top of the figure for each loading-unloading cycle. The plasticity factor $\rho = \Delta X_0/\Delta X$, where ΔX_0 and ΔX are the distances shown in Fig. 3, was then computed according to Equation 2 $\rho = 0.31$. The corrected fracture toughness, computed according to Equation 3 is $K_{IC} = 4.8\,\text{MN} \cdot \text{m}^{-3/2}$.

Fig. 4 shows the average load-displacement curve of 20 specimens. The displacement at the peak load is $d = 0.16$ mm (st. dev. = 0.017, $d_{\max} = 0.19$ and $d_{\min} = 0.13$ mm).

Experimental compliance tests were used to calibrate the short rod CNT. The compliance (the ratio between displacement and load) was related to the dimensionless

TABLE I Coefficients of the fourth degree polynomial which fits the dimensionless compliance C' ($R = 0.98$)

M_0	M_1	M_2	M_3	M_4
− 1935	14569	− 36083	35993	− 9453

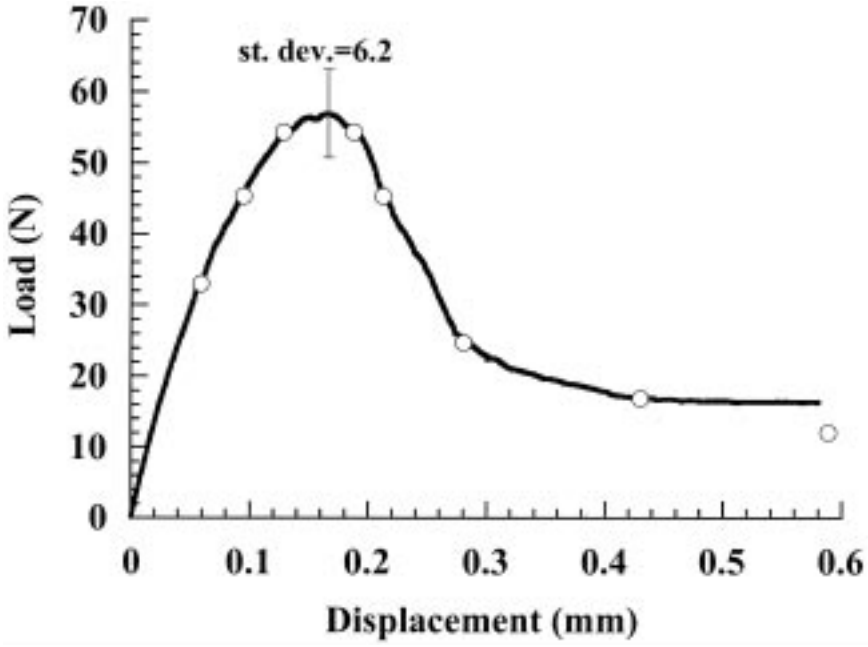

Figure 4 Average load-displacement curve of 20 CNT bone specimens.

crack length measured using XMT images ($\alpha < 0.8$) and video digital images ($\alpha > 0.7$).

Dimensionless compliance, computed according to Equation 4, is related to the crack length. Its behavior is described by the polynomial fitting function (Fig. 5) derived from Equation 5. The polynomial coefficients are shown in Table I. The dimensionless stress intensity factor Y was computed according to Equation 6, and the minimum value of Y is related to the dimensionless crack length $\alpha = 0.47$. Fracture toughness (the critical stress intensity factor) is then computed according to Equation 7: $K_{IC} = 4.9\,\mathrm{MN \cdot m^{-3/2}}$.

Discussions

The advantage of the chevron notch geometry can be seen from a comparison of the theoretical behavior of the CNT and the straight-through crack (STC) specimens [42]: the normalized stress intensity factor (Y) for the STC is a monotonically increasing function of the crack length, while Y is characterized by a function which passes through a minimum as the crack grows in the CNT specimens. This latter behavior is related to the widening of the crack front as it advances along the specimen axis which causes the crack growth to be stable initially [33].

The opening load, applied to the mouth of the specimen, continuously increases with crack length reaching a maximum value. In this phase a steady-state propagating crack is observed even using a force controlled testing machine and brittle materials.

According to Equations 1 and 3 fracture toughness is computed without any information on the crack length. If specimen plasticity is negligible, then the peak load is the only mechanical measure used to compute the critical

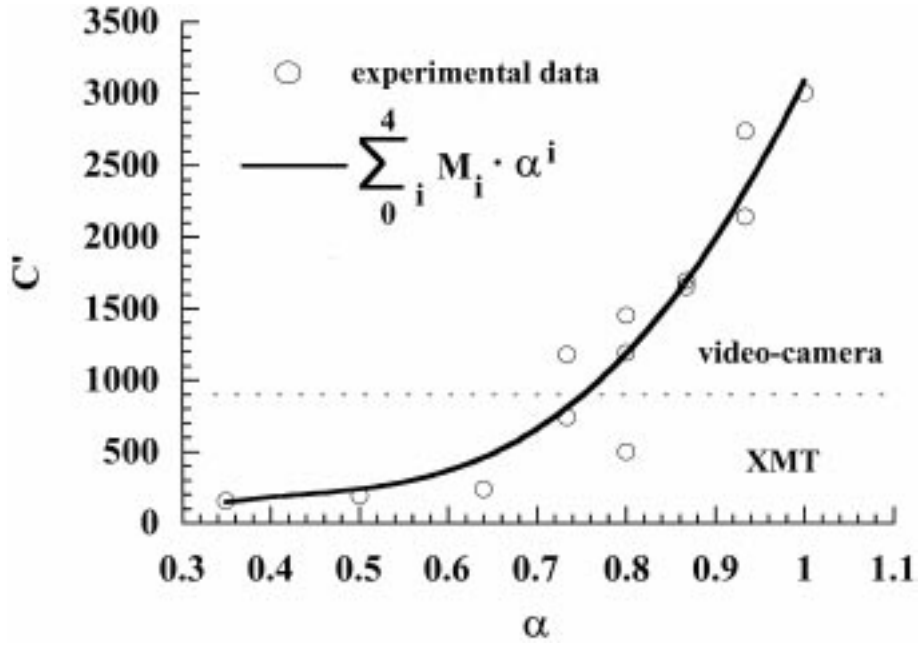

Figure 5 Dimensionless compliance behavior. Experimental data were fitted using a fourth polynomial function.

stress intensity factor. However the price to pay for the easy estimation of fracture toughness is that the crack growth resistance curve (R-curve) has an ''S-shape'' which depends on the chevron-notch geometry [43]. Dimensional requirements [24] are difficult to achieve with bone specimens, because of the curved cross-section of most long bones [25]. Even if geometrical properties of a scale-down specimen are proportional to those of the standard size, the specimen may not belong to the short rod standard family [44] because the chevron slot thickness τ is constrained by the cutting equipment, hence the ratio between τ and the slot bottom geometry (D) is not acceptable. Thus, when using bone specimens, compliance tests for calibration may provide more accurate measurements of the plane-strain stress intensity factor [45].

During the initial loading (Figs 3 and 4) a linear elastic region is characterized by a slope which is related to the elastic modulus of the specimen material [32] and the onset of non linearity occurs when the crack initiates at the point of the V (Figs 6 and 7). The experimental compliance test is complicated by the measurement of the crack length. XMT analysis allowed the carefully measurement of the geometrical properties of the crack at a given stress. The spatial resolution (which refers to the minimum distance in the target that separates distinguishable features in the image) of tomographic images for conventional axial applications is of the order of one millimeter [43] while that of XMT images is a few micrometers.

The XMT data show that when the maximum load is reached the crack length is $\alpha = 0.500(\pm 0.008)$ (Fig. 6). The minimum of the stress intensity factor computed from the R-curve is related to $\alpha = 0.47$. Hence the fracture toughness measurement is made at the time of the maximum load when the crack is already in the central region of the specimen [3, 5]. Thus the fracture toughness measurement (K_{IC}) is related to that of a nearly plane-strain [44] crack growth resistance curve.

Moreover longitudinal and parallel cut XMT slices

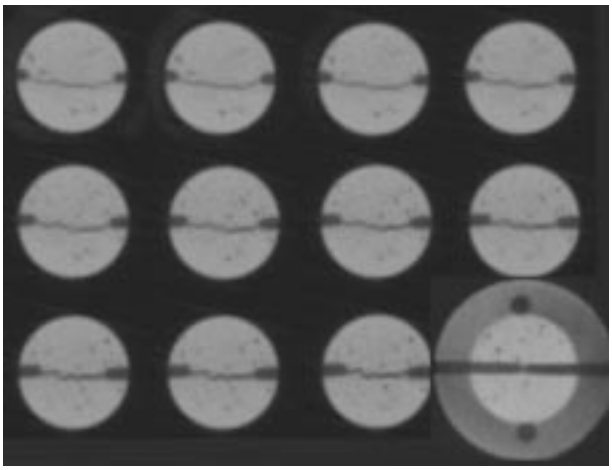

Figure 6 X-ray slices normal to the z axis showing the track of the crack about $\alpha = 0.8$.

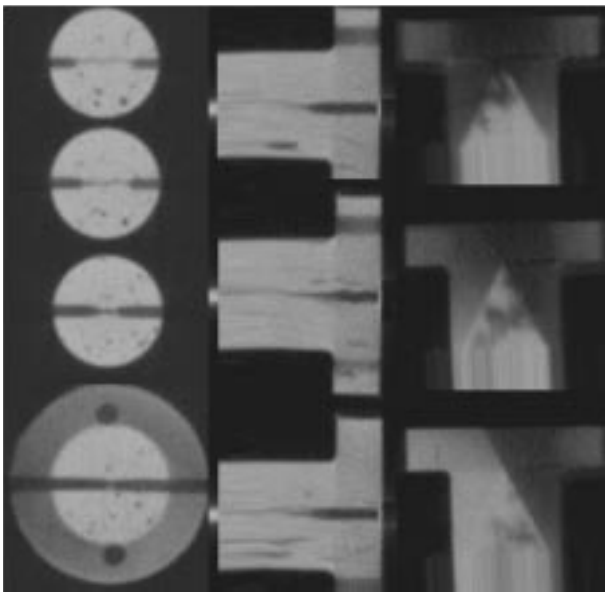

Figure 7 X-ray slices normal to the z axis (first vertical strip) about $\alpha = 0.5$, the second and the third strip are related to longitudinal slices parallel to $\pi_{z,y}$ and $\pi_{z,x}$ respectively.

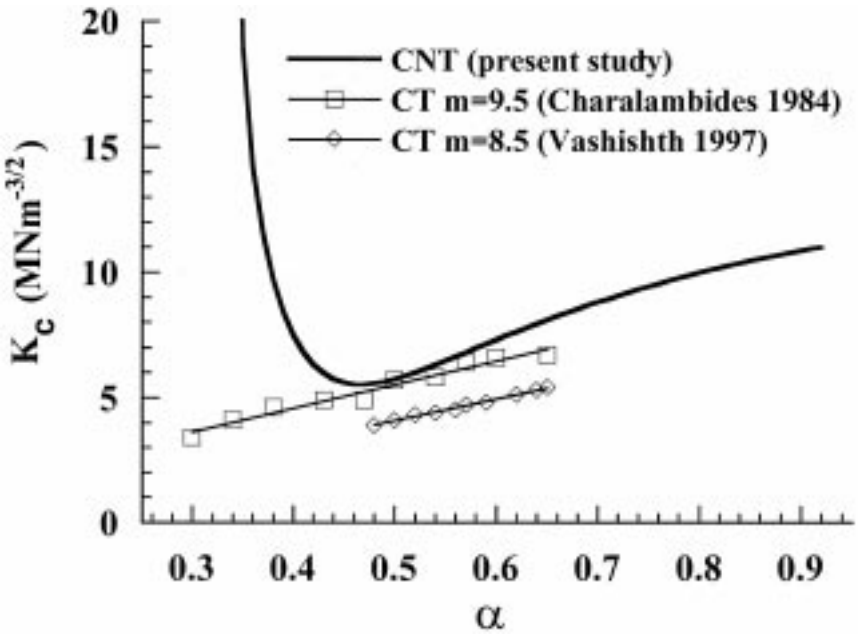

Figure 8 Crack growth resistance curve vs dimensionless crack length related to the CNT and CT specimens.

show that a less dense planar zone, characterized by a lower grey tonality, already extended to the deep edge when the maximum load was reached (Fig. 7). This zone is representative of bone structure arrangement, characterized by a frontal process zone and a significant process zone wake, consistent with the toughening mechanisms in quasi-brittle microcracking solids [4], where toughening effects are mainly produced by the microcracks formed in the wake [46] which causes a redistribution of stresses in the crack-tip region.

The crack growth resistance K_C (fracture toughness) versus the crack extension for CNT specimens is shown in Fig. 8. This behavior is compared to the *R*-curves of slow-stable crack propagation using CT specimens [4, 47] where the coefficients m indicates the slopes of the linear fitting of the *R*-curves. This behavior is affected by toughening mechanism in the process zone wake, where the plastic zone grows as the crack advances absorbing part of the energy available at the tip (Figs 8 and 9) characterising an increase in the closure stress [4] in the crack-wake region as the crack propagates. The effect is the increase of the toughness of the material characterized by a rising *R*-curve [48, 49]. This behavior characterizes even brittle materials such as ceramics [49] that undergo bridging effects when fracturing [43]. Fig. 9 shows macroscopical bridging effects for bovine cortical bone which fractures in the longitudinal direction showing osteon debonding. Each frame is related to the load-displacement conditions shown by the dots on the graph in Fig. 4. Even if the *R*-curve depends on the chevron notch geometry [43] the minimum value of fracture toughness of the CNT specimens falls in an intermediate value between the initial and the plateau values of the R-curves (Fig. 8) which is consistent with fracture behavior of brittle materials [50].

Conclusions

The fracture toughness computed according to the peak load test [32–34] ($K_{IC} = 4.8\,\mathrm{MNm}^{-3/2}$) is consistent with that computed using the experimental compliance test and that derived for bovine cortical bone CT specimens [4]. Fracture toughness of cortical bovine bone for CNT specimens, measured according to Equation 1, yields values that are 40% below the toughness measured with other specimens geometries [31]. If the plasticity correction is used (Equation 3) then the toughness value are in good agreement with CT results [4].

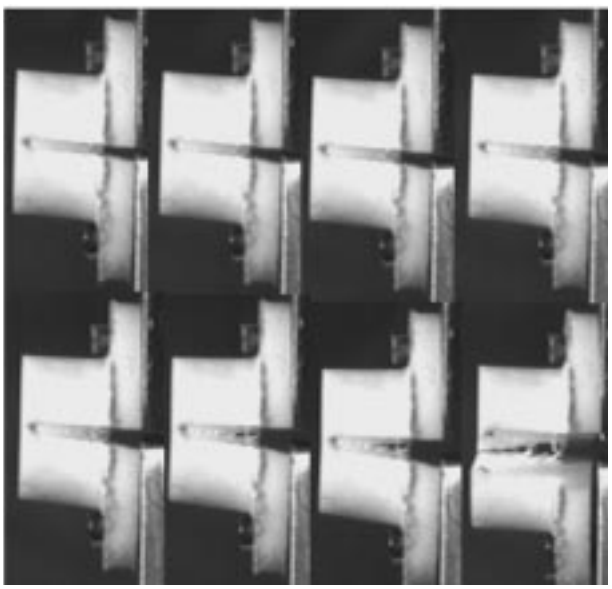

Figure 9 Video camera frames related to the load-displacement conditions expressed by the dots on the graph in Fig. 4.

Acknowledgments

The visit of Roberto De Santis to the IRC in Biomedical Materials was funded by progetto finalizzato MSTA II of the Italian National Research Council. The work at QMW was partly funded by The Special Trustees of the Royal London Hospital. The IRC in Biomedical Materials is funded by a core grant from UK EPSRC.

The authors are grateful to Mr M. Elliot for his assistance with the maching of the specimens and grips.

References

1. R. S. LAKES, S. NAKAMIRA, J. C. BEHIRI and W. BONFIELD, *J. Biomech.* **10** (1990) 967.
2. J. D. CURREY, *J. Microsc. Sci.* **103** (1962) 11.
3. W. BONFIELD and P. K. DATTA, *J. Biomech.* **9** (1976) 131.
4. D. VASHISHTH, J. C. BEHIRI and W. BONFIELD, *ibid.* **30** (1997) 763.
5. T. L. NORMAN, D. VASHISHTH and D. BURT, *ibid.* **28** (1995) 309.
6. F. G. EVANS and R. VINCENTELLI, *ibid.* **2** (1969) 63.
7. D. B. BURR, M. B. SCHAFFLER and R. G. FREDERICKSON, *ibid.* **11** (1988) 939.
8. A. SIMKIN and G. ROBIN, **7** (1974) 183.
9. R. B. MARTIN and D. B. BURR, *J. Biomech.* **15** (1982) 137.
10. X. E. GUO, L. C. LIANG and S. A. GOLDSTEIN, *J. Biom. Engin.* **120** (1998) 112.
11. M. B. SCHAFFER, K. CHOI and C. MILGROM, *Bone* **17** (1995) 521.
12. T. L. NORMAN and Z. WANG, *ibid.* **20** (1997) 375.
13. A. C. COURTNEY, W. C. HAYES and L. J. GIBSON, *J. Biomech.* **29** (1996) 1463.
14. B. MARTIN, *Calc. Tiss. Int.* **53** suppl. 1 (1993) S34.
15. L. E. CLAES, H. J. WILKE and H. KIEFER, *J. Biomech.* **28** (1995) 1377.
16. D. M. ROBERTSON, D. ROBERTSON and C. G. BARRET, *ibid.* **11** (1978) 359.
17. T. M. WRIGHT and W. C. HAYES, *ibid.* **10** (1977) 419.
18. J. C. BEHIRI and W. BONFIELD, *ibid.* **17** (1984) 25.
19. T. L. NORMAN, D. VASHISHTH and D. BURR, *ibid.* **29** (1996) 102.
20. W. BONFIELD, *ibid.* **20** (1987) 1071.
21. J. W. MELVIN and F. G. EVANS, Biomechanics Symposium ASME (New York, 1973) 87.
22. D. MOYLE and A. J. GAVENS, *J. Biomech.* **19** (1986) 919.
23. X. WANG and C. M. AGRAWAL, *J. Biom. Mat. Res.* **33** (1996) 13.
24. ASTM Standards E 399-72, Standard Method of Test for Plane-Strain Fracture Toughness of Metallic materials.
25. J. W. MELVIN, *J. Biomech. Eng.* **115** (1993) 549.
26. J. C. BEHIRI and W. BONFIELD, *J. Biomech.* **22** (1989) 863.
27. G. R. DAVIS and J. C. ELLIOT, *Nucl. Instr. Meth. Phys. Res.* **A394** (1997) 157.
28. W. GRAEFF and K. ENGELKE in ''Microradiography and microtomography'', S. Ebashi, M. Kohc, E. Rubenstein (North Holland, Amsterdam 1991) 361.
29. J. C. ELLIOT, P. ANDERSON, X. J. GAO, F. S. L. WONG, G. R. DAVIS and S. E. P. DOWKER, *J. X-ray Sci. and Tech.* **4** (1994) 102.
30. ASTM Standards B 771-87, Standard Test for Short Rod Fracture Toughness of Cemented Carbides.

31. http ://www.terratek.com7fracto_2.htm
32. D. P. H. HASSELMAN and F. F. LANGE in ''Fracture Mechanics of Ceramics'' Vol. 3, Edited by R.C. Bradt (Plenum Press, New York, 1978) 483.
33. L. M. BARKER, *Int. Fract. Mech.* **9** (1977) 361.
34. L. S. COSTIN, in ''symposium on fracture mechanics for ceramics, rocks and concrete''. Chicago, June 1980 (printed in Baltimora 1981) 169.
35. B. P. FLANNERY, H. W. DECKMAN, W. G. ROBERGE and K. L. D'AMICO, *Science* **237** (1987) 1439.
36. B. P. FLANNERY and W. G. ROBERGE, *J. Appl. Phys.* **62** (1987) 4668.
37. G. R. DAVIS and FERRANTI S. L. WONG, *Physiol. Meas.* **17** (1996) 121.
38. J. C. ELLIOT, G. R. DAVIS, FERRANTI S. L. WONG, STEPHANIE E. P. DOWKER and C. E. MERCER, *Anal. Quimica* **93** (1997) S77.
39. D. T. REILLY, A. H. BURSTEIN and V. H. FRANKEL, *J. Biomech.* **7** (1974) 271.
40. D. T. REILLY and A. H. BURSTEIN, *J. Bone and Joint Surgery* **56-A** (1974) 1001.
41. R. T. BUBSEY, D. MUNZ, W. S. PIERCE and J. L. SHANNON JR., *Int. J. of Fracture* **18** (1982) 125.
42. J. C. NEWMAN, in ''Chevron-Notched Specimens'' (Underwood, Freiman and Baratta editors, printed in Baltimora 1984) 5.
43. T. AKATSU, E. YASUDA and M. SAKAI, in ''Fracture Mechanics of Ceramics'', vol. 11, Ed. R. C. Bradt *et al.* (Plenum Press, New York 1996) 245.
44. L. M. BARKER, *Engng Fract. Mech.* **17** (1983) 289.
45. T. LANG, B. H. HASEGAWA, S. C. LIEW, J. K. BROWN, S. C. BLANKSPOOR, S. M. REILLY, E. L. GINGOLD and C. E. CANN, *J. Nucl. Med.* **33** (1992) 1881.
46. F. G. EVANS and K. T. FABER, *J. of Am. Ceramic Soc.* **67** (1984) 255.
47. B. CHARALAMBIDES, M. Phil. thesis, University of London.
48. T. L. ANDERSON in ''Fracture Mechanics: foundamental and applications'', CRC Press, Boca Raton, F.L., 1990.
49. S. SURESH in ''Fatigue of materials'', Cambridge Univ. Press, D.R. Clarke Ed., Great Britain, 1991.
50. D. MUNZ, R. T. BUBSEY and J. E. SRAWLEY, *Int. Jour. Fract.* **16** (1980) 354–374.

Received 5 April
and accepted 24 August 1999